

Gloria Arancibia · Stephen J. Matthews ·
Paula Cornejo · Carlos Pérez de Arce ·
José I. Zuluaga · Stabro Kasaneva

$^{40}\text{Ar}/^{39}\text{Ar}$ and K–Ar geochronology of magmatic and hydrothermal events in a classic low-sulphidation epithermal bonanza deposit: El Peñon, northern Chile

Received: 20 December 2005 / Accepted: 12 June 2006 / Published online: 27 July 2006
© Springer-Verlag 2006

Abstract The epithermal El Peñon gold–silver deposit consists of quartz–adularia veins emplaced within a late Upper Paleocene rhyolitic dome complex, located in the Paleocene–Lower Eocene Au–Ag belt of northern Chile. Detailed K–Ar and $^{40}\text{Ar}/^{39}\text{Ar}$ geochronology on volcano–plutonic rocks and hydrothermal minerals were carried out to constrain magmatic and hydrothermal events. The Paleocene to Lower Eocene magmatism in the El Peñon area is confined to a rhomb-shaped basin, which was controlled by N–S trending normal faults and both NE- and NW-trending transtensional fault systems. The earliest products of the basin-filling sequences comprise of Middle to Upper Paleocene (~59–55 Ma) welded rhyolitic ignimbrites and andesitic to dacitic lavas, with occasional dacitic dome complexes. Later, rhyolitic and dacitic dome complexes (~55–52 Ma) represent the waning stages of volcanism during the latest Upper Paleocene and the earliest Eocene. Lower Eocene porphyry intrusives (~48–43 Ma) mark the end of the magmatism in the basin and a change to a compressive tectonomagmatic regime. $^{40}\text{Ar}/^{39}\text{Ar}$ geochronology of hydrothermal adularia from the El Peñon deposit yields ages between 51.0 ± 0.6 and 53.1 ± 0.5 Ma. These results suggest that mineralization occurred slightly after the emplacement of the El Peñon rhyolitic dome at 54.5 ± 0.6 Ma ($^{40}\text{Ar}/^{39}\text{Ar}$ age) and was closely tied to later dacitic–rhyodacitic bodies of 52 to 53 Ma (K–Ar ages), probably as short-lived pulses related to single volcanic events.

Editorial handling: R. King

G. Arancibia (✉) · S. J. Matthews · P. Cornejo · C. P. de Arce
Servicio Nacional de Geología y Minería,
Avda. Santa María 104,
Santiago, Chile
e-mail: gloarancibia@123.cl
Tel.: +56-2-2385276
Fax: +56-2-2385332

J. I. Zuluaga · S. Kasaneva
Compañía Minera Meridian Limitada,
Avenida General Velásquez 890, Oficina 670,
Antofagasta, Chile

Keywords K–Ar and $^{40}\text{Ar}/^{39}\text{Ar}$ geochronology · Epithermal gold · Low-sulphidation · Chile

Introduction

Several studies show that hydrothermal mineral deposits are closely related in space and time to pulses of volcanism and plutonism, particularly in the later phases of such pulses (e.g., McKee and Noble 1989; Cathles et al. 1997; Chesley et al. 1993). Geological evidence and modelling studies generally suggest that hydrothermal activity occurs either as short-lived pulses lasting less than 100,000 years or as long-lived systems of ~1 Ma (e.g., Cathles et al. 1997). In almost all cases, hydrothermal circulation, geothermal activity, and magmatic event are closely related in time and space, and long-lived systems consist of a series of short-lived pulses of intrusion and hydrothermal circulation (Cathles et al. 1997).

Epithermal gold deposits in the Central Depression of northern Chile are associated with Cretaceous to Paleogene magmatic arcs which form NS trending belts, parallel to the present-day coastline. The formation of a Paleocene–Lower Eocene Au–Ag epithermal metallogenic belt has been documented by several studies (e.g., Sillitoe et al. 1991; Sillitoe and McKee 1996, and references therein) (Fig. 1).

The epithermal El Peñon Au–Ag deposit, located in the center of the metallogenic belt, was emplaced within a late Upper Paleocene rhyolitic dome complex, emplaced itself along a NE trending fracture zone which affects a Middle to Upper Paleocene volcanic sequence (Fig. 2). The deposit comprises of at least four epithermal quartz–adularia veins, ranging between <50 cm to 22 m in width. Measured, indicated, and inferred resources in 2004 were 8.4 million metric tons at 14 g/t Au and 234 g/t Ag, including the bonanza-grade Quebrada Colorado vein (Warren et al. 2004). This deposit is the most important bonanza Au–Ag deposit in the belt, and contains more than half of its reported gold resource.

Preliminary adularia K–Ar dating yielded ages between 59.4 ± 1.4 and 53.5 ± 2.2 Ma (Pérez 1999). $^{40}\text{Ar}/^{39}\text{Ar}$ data on

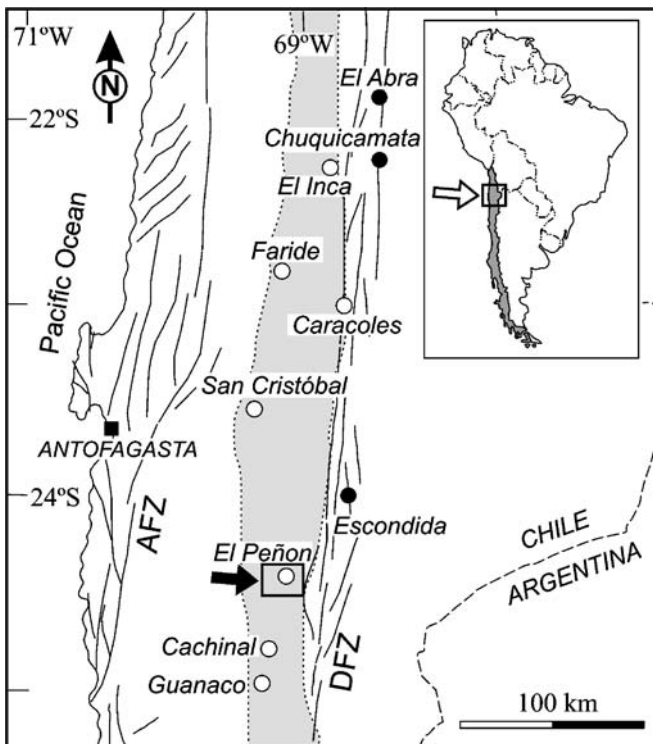


Fig. 1 Paleocene–Eocene epithermal belt (gray zone) developed in northern Chile. White circles represent Au–Ag deposits and black circles Cu–porphyry deposits. Study area outlined by rectangle. AFZ Atacama Fault Zone; DFZ Domeyko Fault Zone

adularia cited by Warren et al. (2004), suggest mineralization ages of 52 to 53 Ma. In this study, we report new K–Ar and $^{40}\text{Ar}/^{39}\text{Ar}$ ages to constrain magmatic events in the El Peñon area and the age of hydrothermal mineralization, focussing our discussion on the relationship between magmatism and mineralization events.

Geological setting

The El Peñon mine ($24^{\circ}20'S$) lies within the Central Depression of northern Chile. This geographical feature corresponds mainly to a series of Late Cretaceous to Lower Eocene basins which are bounded to the west by the Coastal Cordillera, comprising Paleozoic to Lower Cretaceous rocks (e.g., Scheuber and González 1999), and to the east by the Precordillera, which corresponds to the Eocene–Early Oligocene magmatic arc emplaced over Late Paleozoic to Jurassic sequences (e.g., Marinovic et al. 1995; Tomlinson and Blanco 1997). Two major structures bound the basin: an unnamed fault system to the west (locally, the Dominador F.Z.) and the Domeyko Fault System to the east (Fig. 1). In the study area, the Central Depression *sensu strictu* is a narrow feature, about 20 km in width, with a general trend to the NNE. The western boundary comprises of Paleozoic basement and overlying Mesozoic sequences to the west of the Dominador Fault

System, whereas the Cerro Paisaje Fault System defines its eastern limit (Fig. 2).

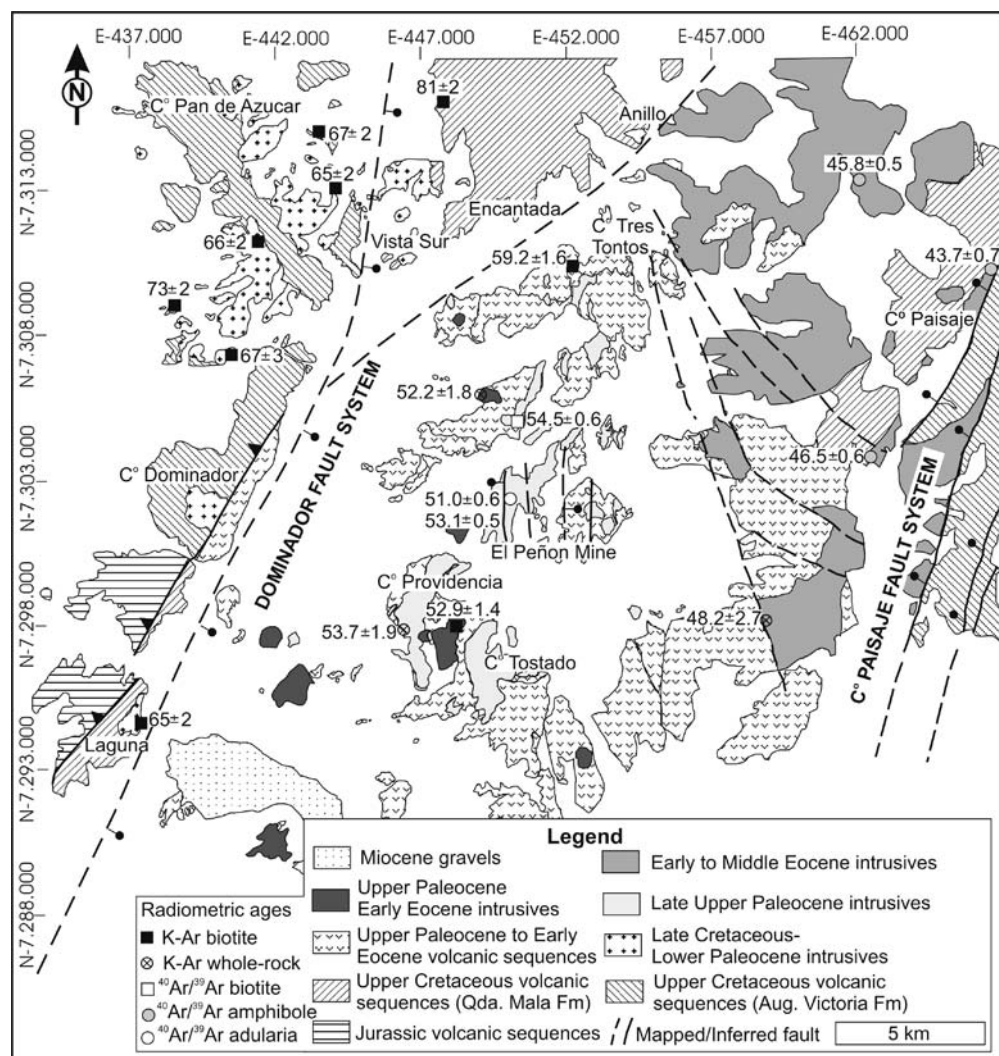
Jurassic volcanic units are identified to the south of Cerro Dominador and consist mostly of rhyolitic welded ignimbrites and minor andesite lavas (Fig. 2). To the north, a dominantly ignimbritic sequence is assigned to the Middle to Upper Cretaceous Augusta Victoria Formation as defined by García (1967). A continental volcanic-sedimentary sequence is present to the north of Cerro Tres Tontos, characterized by tight folding, faulting, and strong argillic alteration. The unit consists of highly welded rhyodacitic and rhyolitic ignimbrites, andesite lavas, volcaniclastic breccias, fine-grained fluvio–lacustrine quartz–feldspathic sandstones, and small andesitic lithics. This unit was assigned by Marinovic et al. (1995) to the Aeropuerto Formation; however, in this study, is assigned to the Upper Cretaceous Quebrada Mala Formation, based on descriptions of intrabasin volcanic sequences for the Central Depression between the Altamira ($25^{\circ}30'S$) and El Peñon areas (Cornejo et al. 2003), and to the north, in the Pampa Union area (Marinovic and García 1999). A series of late Upper Cretaceous plutons intrudes the sequences along the western margin of study area (Fig. 2). These intrusions comprise diorites, quartz monzodiorites, granodiorites, and rare gabbros, and form small sills, stocks, and larger irregular plutons.

The Cretaceous sequences were strongly deformed in a Lower Paleocene deformation phase, termed the “K–T deformation” by Cornejo et al. (2003), equivalent to the “Incaic 1” phase of Sébrier et al. (1988) and Mc Kee and Noble (1989), so that Middle to Upper Paleocene volcanic sequences, which comprise the basin-fill, overlie these rocks via an angular unconformity. The basin-fill sequences correspond to a sequence of basaltic, andesitic, rhyolitic, and dacitic rocks, associated with an extensional–transtensional tectonic environment, during the Upper Paleocene–Early Eocene (e.g., Cornejo and Matthews 2001; Cornejo et al. 2003). In the Vista Sur–La Encantada area, the NNE-trending Dominador fault system swings to the NE and the basin margin is controlled by a NE-trending transtensional fault which places basin-filling sequences against the folded Quebrada Mala Formation. To the north of the study area, the basin margin returns to a northerly trend. The eastern margin of the basin is defined by the Cerro Paisaje fault system, which shows later reactivation as a reverse or transpressional fault system.

Early to Middle Eocene intrusive complexes constitute the younger intrusive rocks in the study area (Cornejo and Matthews 2001). These intrusions comprise dioritic and quartz monzodioritic plutons and andesitic, monzonitic, and dacitic porphyries, which are emplaced as large sills or laccoliths into the base of the Upper Paleocene volcanic sequences located NE of the El Peñon deposit. These intrusive complexes postdate the end of Upper Paleocene to Early Eocene volcanism and continue until the beginning of the Incaic compressive phase in the Middle Eocene in northern Chile.

Finally, an extensive cover of Miocene to Quaternary alluvial gravels is present throughout the Central

Fig. 2 Simplified geological map of the El Peñon deposit and surrounding areas (modified from Arancibia et al. 2006). K–Ar and $^{40}\text{Ar}/^{39}\text{Ar}$ ages of analytical data presented in this paper



Depression. In the El Peñon area, these gravels have not been studied in detail because they are not deeply incised as in other areas to the south and north (Fig. 2).

Analytical methods

Samples to be analyzed by the K–Ar and $^{40}\text{Ar}/^{39}\text{Ar}$ methods were collected from plutonic and volcanic rocks in the El Peñon area. Amphibole and biotite from the crushed 500–250 μm fraction were separated by hand picking under binocular microscope and cleaned in distilled water. K–Ar, $^{40}\text{Ar}/^{39}\text{Ar}$, and X-ray diffraction analysis were carried out in the Laboratorio de Geocronología of Servicio Nacional de Geología y Minería, Chile. Details of the analytical procedures are given in Arancibia et al. (2006).

To date hypogene mineralization, adularia-quartz aggregates were obtained from crushed mineralized veins. The aggregates were attacked with a HF and CoNO_3 saturated solution for 40 s, to dye the adularia grains that were then selected by hand picking under a binocular microscope. The adularia grains were then discolored by

ultrasonic cleaning in distilled water for 1 to 2 days. Once the separate was cleaned, five to ten grains from each sample were prepared for SEM and electron microprobe analysis. Spot chemical analyses were carried out with a CAMECA SU-30 SEM-probe (Universidad de Chile). Samples were studied under both secondary (SE) and backscattered electron (BSE) modes to characterize the morphology, habits, grain size of the phases, and detect any possible intergrown minerals. Polished adularia samples were quantitatively analyzed with the SEM-probe equipped with a wavelength dispersive spectrometer and Cameca SX-50 software. The beam current was 10 nA, accelerating voltage was 15 kV and the beam diameter was 2 μm . Natural minerals were used as standards.

For the $^{40}\text{Ar}/^{39}\text{Ar}$ method, Ca-bearing samples (i.e., amphibole) required a cooling period of 2–3 half lives ($t_{1/2} \sim 35$ days) to reduce the amount of radioactive ^{37}Ar generated during irradiation. A representative value of a discrimination factor during analysis was $D = 1.00400 \pm 0.00020$ ($D = [295.5 / ({}^{40}\text{Ar} / {}^{39}\text{Ar})_m]^{0.25}$). Reactor isotope production ratios were determined using fluorite, synthetic kalsilite (potassium aluminum silicate), and Ca–S glasses

and correspond to: $(^{40}\text{Ar}/^{39}\text{Ar})\text{K}=0.0014057\pm 0.0003348$; $(^{36}\text{Ar}/^{37}\text{Ar})\text{Ca}=0.0003330\pm 0.0000012$; and $(^{39}\text{Ar}/^{37}\text{Ar})\text{Ca}=0.0007780\pm 0.0000033$. Representative blanks obtained during the analysis were as follows: $^{40}\text{Ar}=1.10\times 10^{-16}$, $^{39}\text{Ar}=3.15\times 10^{-19}$, $^{38}\text{Ar}=1.48\times 10^{-19}$, $^{37}\text{Ar}=5.49\times 10^{-19}$, and $^{36}\text{Ar}=2.86\times 10^{-19}$ mol. Age uncertainties are presented at the 2σ levels and J values are given for each sample.

Geology and geochronology of the El Peñon area

Geochronology of magmatic events

The El Peñon deposit was mapped by geologists of the Meridian Gold Company and the compiled regional geology was documented by Warren et al. (2004). This work has been updated and slightly modified by our new ages and mapping. K–Ar (sample DCM-027) and $^{40}\text{Ar}/^{39}\text{Ar}$ (sample DCM-17) analytical data summarized by Cornejo et al. (2003) are included in Tables 1 and 2 and Fig. 2.

A K–Ar age of 81 ± 2 Ma was obtained in this study on a slightly chloritized biotite from a very crystal-rich biotite–sanidine–quartz rhyolite ignimbrite (sample DCM-754, Table 1), located to the north of the study area. Both the age and the lithological characteristics of this unit are consistent with Upper Cretaceous intrabasin volcanic sequences, assigned to the Quebrada Mala Formation (Fig. 2). Geochronological K–Ar data for late Upper Cretaceous plutons in the Pan de Azúcar and Laguna areas

northwest of the El Peñon mine, give ages ranging between 65 ± 2 and 73 ± 2 Ma (Table 1, Fig. 2).

Upper Paleocene basin-fill volcanic sequences are extensively distributed in the El Peñon area and a K–Ar age of 59.2 ± 1.6 Ma from biotite in ignimbrite from Cerro Tres Tontos (sample DCM-027, Cornejo et al. 2003) was obtained (Table 1, Fig. 2). The volcanic sequences were intruded by a series of dome complexes, which are composed mainly of rhyolitic domes and subordinate later dacitic–rhyodacitic bodies. The rhyolitic domes (i.e., El Peñon Dome) correspond to much of the volume of magmatic rocks in the El Peñon deposit and constitute the host rock of mineralized veins. $^{40}\text{Ar}/^{39}\text{Ar}$ analysis from a fluidal biotite rhyolite (DCM-017, Cornejo et al. 2003) north of the El Peñon mine (Table 2, Fig. 2) yields a well-defined plateau age of 54.5 ± 0.6 Ma (Fig. 3a). Younger ages were obtained from the first low-temperature steps and these are excluded from the isotope correlation analysis, resulting in an isochron age indistinguishable from the plateau age (Table 2). The later dacitic bodies were sampled at Cantera, north of the El Peñon mine, and in the Cerro Providencia area. K–Ar ages of 52.9 ± 1.4 Ma (biotite), 52.2 ± 1.8 Ma (whole rock), and 53.7 ± 1.9 Ma (whole rock) were obtained (Table 1, Fig. 2).

Early to Middle Eocene intrusive complexes were dated by K–Ar for a diorite to the east of Cerro Tostado (Table 1, Fig. 2) at 48.2 ± 2.7 Ma (whole-rock), and two additional $^{40}\text{Ar}/^{39}\text{Ar}$ ages of amphiboles from the Cerro Paisaje area show well-defined plateaus at 45.8 ± 0.5 and 43.7 ± 0.7 Ma, respectively (Fig. 3b,c), concordant with calculated

Table 1 K/Ar analytical data of samples from the El Peñon area

Sample	Location	UTM N	UTM E	Description	Material	K (%)	Ar rad nl/g	Ar atm. (%)	Age (Ma) $\pm 2\sigma$
DCM-754	Encantada	7316127	447770	Rhyolitic sanidine and biotite ignimbrite	Biotite	6.315	20.319	44	81 ± 2
DCM-633	Pan de Azúcar	7313071	444078	Pyroxene and biotite monzodiorite	Biotite	7.146	18.369	11	65 ± 2
DCM-652	Pan de Azúcar	7311000	443202	Pyroxene and biotite monzodiorite	Biotite	5.643	14.749	17	66 ± 2
DCM-663	Pan de Azúcar	7309209	438118	Pyroxene, biotite, and amphibole fine-grained diorite	Biotite	6.407	18.521	12	73 ± 2
DCM-666	Pan de Azúcar	7307315	440567	Pyroxene, biotite, and amphibole diorite	Biotite	3.888	10.268	43	67 ± 3
DCM-021	Pan de Azúcar	7314954	443291	Pyroxene and biotite quartz monzodiorite	Biotite	7	18.51	13	67 ± 2
DCM-529	Laguna	7295055	437424	Diorite	Biotite	7.055	18.209	14	65 ± 2
DCM-027	Tres Tontos	7310628	452136	Rhyolitic biotite ignimbrite	Biotite	6.81	16.92	33	59.2 ± 1.6
DCM-558	Co Tostado	7298128	448229	Biotite and hornblende rhyodacite	Biotite	7.06	14.74	27	52.9 ± 1.4
DCC-219	Cantera	7305931	449250	Hornblende and pyroxene dacitic sill	Whole rock	2.46	5.06	30	52.2 ± 1.8
DCC-370	Co Providencia	7297951	446178	Trachytic pyroxene and olivine intrusive	Whole rock	1.693	3.588	38	53.7 ± 1.9
DCM-030	E of Co Tostado	7298336	458832	Pyroxene and biotite diorite	Whole rock	1.82	3.47	64	48.2 ± 2.7

Table 2 $^{40}\text{Ar}/^{39}\text{Ar}$ analytical data of samples from magmatic rocks in the El Peñon area

Step	Laser Pwr	$^{36}\text{Ar}/^{39}\text{Ar}$	$^{37}\text{Ar}/^{39}\text{Ar}$	$^{38}\text{Ar}/^{39}\text{Ar}$	$^{40}\text{Ar}^*/^{39}\text{Ar}$	Mol ^{39}Ar	$^{40}\text{Ar}^*$ (%)	Age (Ma)	$\pm (2\sigma)$
DCM-017 (biotite from fluidal biotite rhyolite), (7305052N, 450295E)									
A	2	0.359	0.054	0.041	11.859	0.005	10.100	35.42	2.40
B	3	0.090	0.045	0.044	15.995	0.007	37.600	47.62	1.65
C	4	0.048	0.058	0.052	16.959	0.008	54.400	50.45	0.83
D	5	0.030	0.044	0.042	17.143	0.010	65.700	50.99	0.65
E	6	0.024	0.034	0.050	18.323	0.012	72.200	54.44	0.52
F	8	0.015	0.032	0.052	18.230	0.045	80.800	54.17	0.24
G	10	0.012	0.037	0.052	18.312	0.072	83.300	54.41	0.23
H	12	0.009	0.025	0.052	18.411	0.060	87.700	54.70	0.23
I	14	0.009	0.034	0.050	18.548	0.071	87.800	55.10	0.41
J	16	0.009	0.054	0.051	18.320	0.075	87.400	54.44	0.15
K	19	0.009	0.114	0.052	18.296	0.113	87.100	54.36	0.15
L	22	0.007	0.075	0.054	18.391	0.113	89.900	54.65	0.11
M	28	0.006	0.053	0.054	18.335	0.076	91.600	54.48	0.18
Plateau age 54.5±0.6 Ma (96% released gas); MSWD=0.00; $J=0.0016682\pm 0.0000087$									
Inverse isochron age 54.7±0.6 Ma, $n=9$, $^{40}\text{Ar}/^{39}\text{Ar}$ intercept 287±7, MSWD=0.83									
DCM-618 (amphibole from dacytic pyroxene–biotite–hornblende porphyry), (7313243N, 462249E)									
A	5	2.602	5.914	0.158	24.176	0.001	3.000	42.88	13.41
B	10	0.570	12.220	0.214	26.705	0.003	13.700	47.30	2.03
C	13	0.012	14.034	0.253	25.864	0.025	90.400	45.83	0.29
D	16	0.012	13.370	0.250	25.820	0.040	90.200	45.76	0.22
E	19	0.006	13.563	0.251	25.888	0.046	95.600	45.87	0.17
F	30	0.007	13.505	0.245	25.771	0.055	94.700	45.67	0.21
Plateau age 45.8±0.5 Ma (100% released gas); MSWD=0.49; $J=0.0009925\pm 0.0000052$									
Inverse isochron age 45.8±0.6 Ma, $n=6$, $^{40}\text{Ar}/^{39}\text{Ar}$ intercept 296.3±1.7, MSWD=0.24									
DCM-475 (amphibole from hornblende–pyroxene andesitic porphyry), (7310710N, 461675E)									
A	5	2.547	2.471	0.027	5.168	0.001	0.700	10.65	8.56
B	10	0.397	12.371	0.178	19.135	0.003	14.000	39.11	2.45
C	13	0.024	12.123	0.241	21.355	0.045	76.300	43.59	0.34
D	16	0.011	12.375	0.220	21.433	0.065	88.800	43.75	0.17
E	19	0.007	11.594	0.211	21.343	0.099	93.000	43.57	0.14
F	22	0.006	12.266	0.221	21.422	0.047	94.900	43.72	0.17
G	25	0.018	15.458	0.210	21.812	0.001	82.900	44.51	1.96
Plateau age 43.7±0.7 Ma (100% released gas); MSWD=0.95; $J=0.0011425\pm 0.0000088$									
Inverse isochron age 43.7±0.8 Ma, $n=5$, $^{40}\text{Ar}/^{39}\text{Ar}$ intercept 296±10, MSWD=0.37									
DCM-455 (amphibole from porphyric pyroxene–biotite–hornblende monzodiorite), (7303653N, 462450E)									
A	5	0.194	0.146	0.089	32.699	0.017	36.300	73.80	0.66
B	10	0.091	0.825	0.061	53.284	0.016	66.400	118.77	0.52
C	13	0.028	10.412	0.090	21.755	0.039	73.400	49.44	0.33
D	16	0.013	9.798	0.120	20.410	0.057	85.900	46.42	0.26
E	19	0.012	7.179	0.121	20.491	0.031	86.500	46.60	0.21
F	22	0.009	7.175	0.160	20.331	0.015	90.100	46.24	0.51
G	30	0.009	6.340	0.119	15.505	0.029	87.300	35.37	0.17
Plateau age 46.5±0.6 Ma (51% released gas); MSWD=0.54; $J=0.001274\pm 0.0000062$									
Inverse isochron age 44.6±1.0 Ma, $n=4$, $^{40}\text{Ar}/^{39}\text{Ar}$ intercept 376±12, MSWD=0.38									

Data in italics were excluded in inverse isochron analysis

Laser Pwr Power of laser in watt

 $^{40}\text{Ar}^*$ is radiogenic ^{40}Ar

isochron ages (Table 2). A third sample exhibits a disturbed age-spectrum, although a plateau age of 46.5 ± 0.6 Ma with 51% of the released gas is obtained (Fig. 3d). Slightly younger isochron ages are obtained when the A and B steps are excluded (Table 2).

Mineralization

Au–Ag mineralization in the El Peñon deposit is restricted to adularia–quartz veins, hydrothermal breccias, and minor quartz stockwork. Hydrothermal quartz, adularia, carbonates and sulfides were deposited directly from solution, filling open spaces as veins and vugs, and as replacement minerals in altered rocks surrounding the mineralized veins (Warren et al. 2004). The El Peñon vein corridor is defined by fault structures which strike N–S and dip steeply to the east and west, as well as NE-trending connective structures which dip steeply northwards. These structures contain at least four distinct veins: Quebrada Orito, Quebrada Colorado, Cerro Martillo, and Discovery Wash. The veins are hosted within the El Peñon Dome complex, which intrudes pyroclastic and intermediate-composition lava flow units.

Quartz–adularia veins display a variety of typical open-space filling vein textures. Microcrystalline to coarse-grained quartz is found in crustiform, colloform, saccharoidal, comb, and bladed carbonate-replacement forms. The quartz vein material is variable in color, including greenish, light to dark gray, amethystine, white, and translucent. Carbonates were originally a common constituent of the veins, but were either replaced by quartz or removed by supergene leaching in the oxidized zone

(Robbins 2000). Adularia generally occurs as millimeter-scale bands of very fine to fine-grained, clear, white, or light pink crystals. Some bands appear to be completely composed of iron ± manganese oxides, possibly after Fe- and Mn-rich carbonates. Limited drill intercepts at deeper levels (mostly below 1,500 m.a.s.l.) consist of banded and brecciated quartz, adularia, and massive, bladed, and acicular Ca-, Fe-, Mn-, and Mg-bearing carbonates minerals, with pyrite, chalcopyrite, sphalerite, and galena and minor native gold and silver sulfosalts. Pyrite and chalcopyrite are generally more abundant than sphalerite and galena, but sphalerite or galena may locally predominate (Warren et al. 2004).

Pervasive supergene oxidation extends to 400 m below the present surface. Ore minerals observed in oxidized veins consist of electrum (mostly 40–60 wt% Au), acanthite, gold, silver, silver sulfosalts, silver halides, and rarely pyrite, chalcopyrite, and galena. The most common relict sulfides are pyrite and chalcopyrite. Kaolinite, gypsum, alunite, and jarosite are mostly products of supergene weathering and occur along fractures and in vugs. Pervasive iron- and manganese-oxides (hematite, goethite, pyrolusite, cryptomelane, and coronadite) are mainly associated with minor fault breccias that cut all systems. $^{40}\text{Ar}/^{39}\text{Ar}$ dating of supergene minerals gives ages between ca. 27 and 14 Ma for alunite and between ca. 14 and 9 Ma for K-bearing Mn-oxides (Arancibia et al. 2006).

Previous studies (e.g., Warren et al. 2004) document fluid inclusion homogenization temperatures and final ice melting temperatures, measured for primary and a few pseudosecondary liquid-rich inclusions in samples of vein quartz from El Peñon deposit. Results indicate vein deposition from a dilute fluid at temperatures of 230 to

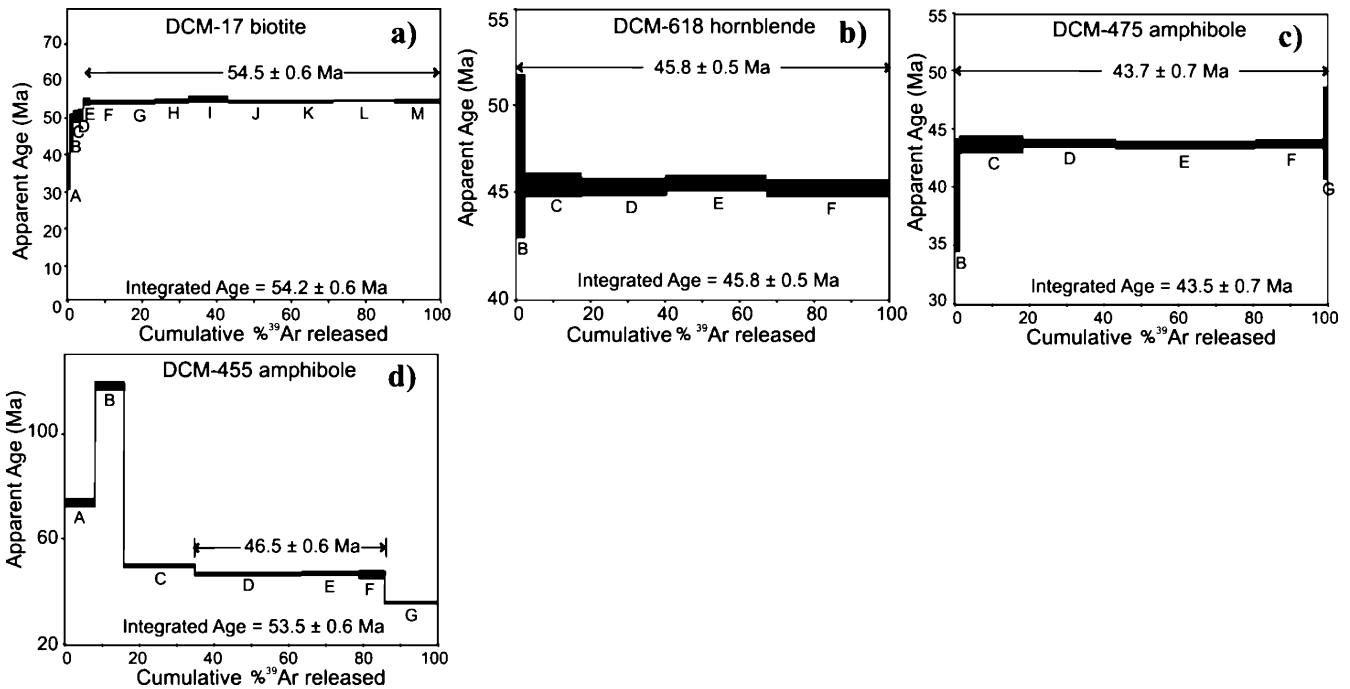


Fig. 3 Conventional $^{40}\text{Ar}/^{39}\text{Ar}$ age spectra of samples from magmatic rocks

260°C and low apparent salinities are explained either by dissolved salts or dissolved gases, most likely CO₂. Minimum depth of formation was 400 m below the paleo water table, with at least 300 m of material having been eroded down to the current surface.

⁴⁰Ar/³⁹Ar geochronology of hydrothermal mineralization

Adularia is a morphologically distinctive variety of potassium feldspar, typical of low-temperature hydrothermal environments (e.g., Dong and Morrison 1995). In El Peñon, this mineral was deposited directly with quartz on the edge of quartz veins close to the wall-rock contacts, probably due to the reaction between wall rocks and hydrothermal fluids. These veins contain the principal concentration of native gold and silver sulfosalts in the deposit, and dating adularia precipitation is the best way to estimate the age of vein formation and hypogene mineralization. Adularia is paragenetically associated with ore mineralization and its closure temperature for the ⁴⁰Ar/³⁹Ar system of 150–380°C (McDougall and Harrison 1999) is similar to the estimated temperature range of vein formation from fluid inclusion studies (230–260°C) (Warren et al. 2004).

Samples of adularia-quartz aggregates were obtained from crushed roses (Fig. 4a), banded veins and matrices of hydrothermal breccias. Separated adularia generally displays a very fine to fine grain size (<1 mm), white to gray color and euhedral rhombic to tabular forms under the microscope (Fig. 4b). In some cases, adularia is partially altered to kaolinite or illite; thus, the cleaning and SEM-EMPA analyses of samples play a fundamental role to avoid the presence of contaminants in ⁴⁰Ar/³⁹Ar analyses. Representative EMPA analyses of adularia are given in Table 3. Seven samples of adularia were analyzed by the ⁴⁰Ar/³⁹Ar method. Conventional age-spectrum plots and isotopic data are presented in Fig. 5 and Table 4, respectively.

Well-defined plateau ages (at least 50% of released ³⁹Ar) beginning from the second or third step in the spectrum give ages of 51.0±0.6 Ma (DCA-11), 52.8±0.8 Ma (DCM-5A), 52.6±0.3 Ma (DCA-12), 53.1±0.5 Ma (DCM-04A), 52.8±0.6 Ma (DCA-17B), and 52.9±0.6 Ma (DCA-17A) (Fig. 5a–f). For samples DCA-11 and DCM-5A, the ³⁶Ar/⁴⁰Ar vs ⁴⁰Ar/³⁹Ar isotope-correlation analysis shows ⁴⁰Ar/³⁶Ar intercept values close to the ⁴⁰Ar/³⁶Ar atmospheric ratio (295.5); thus, the isochron ages are concordant with plateau and integrated ages (Table 4), and they represent the best age estimate for adularia formation. In samples DCA-12 and DCM-4A, isotope-correlation diagrams show an excess argon component (⁴⁰Ar/³⁶Ar intercept values of 1,100±200 and 730±40) (Table 4). Because the released gas has a high radiogenic component (clustering of data on the abscissa), isochron and plateau ages are indistinguishable within error and they are interpreted as maximum ages. For samples DCA-17B and DCA-17A, ³⁶Ar/⁴⁰Ar vs ³⁹Ar/⁴⁰Ar isotope-correlation

diagrams cannot be constructed. However, plateau ages are consistent with the other samples and the spectra do not show evidence for significant excess argon.

Sample DCA-14 shows a disturbed spectrum (Fig. 5g) and an inverse isochron diagram cannot be constructed; thus, it does not yield reliable age information. Possible illite in fractures and/or fluid inclusions in contaminant quartz may be the reason for the perturbed spectra.

Discussion and conclusions

Regional magmatic events

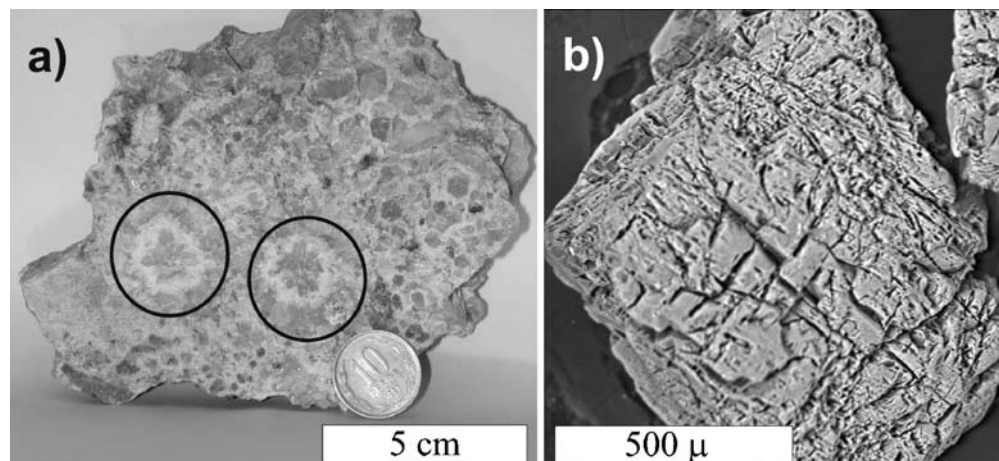
Epithermal deposits in the Paleocene Belt of northern Chile are associated with Upper Paleocene to Early Eocene magmatism, developed within the Central Depression. The Upper Paleocene was characterized by the formation of rhomb-shaped basins in a transtensional tectonic environment (e.g., Cornejo and Matthews 2001; Cornejo et al. 2003). These basins were emplaced largely over the site of the inverted Campanian–Maastrichtian basin, and were controlled by N–S trending normal and transtensional faults and both NE- and NW-trending transtensional fault systems. Within the basin, N–S trending normal faults, probably listric in part, formed small horsts and grabens and caused changes in the thickness of the basin-filling units (i.e., they are growth faults). Commonly, individual ignimbrite flows show thickness variations across these structures, indicating that volcanism and fault movements were contemporaneous.

Upper Cretaceous and Early Eocene magmatism were documented along the western and eastern boundaries of the basin, respectively. The basin-filling sequences were dominantly volcanic and exclusively continental. The earliest products, comprise of Middle Paleocene welded rhyolitic ignimbrites and andesitic to dacitic lavas, with occasional dacitic dome complexes, and were erupted at ~59 Ma (K–Ar ignimbrite). Later, rhyolitic and dacitic dome complexes (~55–52 Ma) represent the waning of volcanism during the latest Upper Paleocene and the earliest Eocene in the basin.

In the El Peñon area, faults that place the Paleocene and Early Eocene volcanic stratigraphy against older (late Upper Cretaceous) and younger intrusive rocks (Early Eocene) in the western and eastern parts, respectively, were also likely active as basin bounding structures (Cornejo et al. 2003). Older intrusive rocks in the western part of the El Peñon area were emplaced between ~73–65 Ma into the Upper Cretaceous extrabasin and intrabasin volcanic sequences to the north and northwest of the El Peñon mine. Folding and faulting of the Upper Cretaceous intrabasin volcanic sequences (Quebrada Mala Formation) occurred during the Lower Paleocene compressive phase.

Younger intrusive rocks in the eastern part of the El Peñon deposit were emplaced almost exclusively into Upper Paleocene volcanic sequences and represent a prolonged period of magmatic activity during the Lower Eocene. Two main events are inferred from petrographic

Fig. 4 **a** Rose texture of quartz-adularia veins from the El Peñon deposit. **b** Backscattered electron image of adularia, displaying tabular crystal with fractures and cavities previously filled with very fine-grained phases



studies and K–Ar and $^{40}\text{Ar}/^{39}\text{Ar}$ geochronology. The earliest event, at ~48–46 Ma, comprises dioritic and quartz monzodioritic plutons crystallized from relatively “dry”,

mafic magmas located immediately to the east of El Peñon. A late intrusive event at ~46–43 Ma, comprises diverse porphyry intrusions (pyroxene hornblende andesite por-

Table 3 Representative electron microprobe analyses of hydrothermal adularia from the El Peñon mine

Sample	DCM-04A	DCM-04A	DCM-05A	DCM-05A	DCA-011	DCA-011	DCA-17A	DCA-17A	DCA-17A	DCA-12	DCA-12	DCA-14	DCA-17B	DCA-17B
Beam size	15	15	15	15	15	15	15	15	15	15	15	2	15	15
Analysis	2–7	2–10	5–26	9–30	11–32	13–34	18–39	19–40	23–44	28–49	30–51	36–57	2–61	5–63
SiO ₂	65.04	65.63	64.99	65.39	63.93	64.47	64.44	64.33	64.05	64.75	64.86	66.70	64.88	64.77
TiO ₂	0.00	0.03	0.00	0.00	0.03	0.03	0.03	0.00	0.03	0.03	0.13	0.00	0.00	0.05
Al ₂ O ₃	17.14	17.03	17.49	17.08	18.23	17.89	17.63	17.81	17.58	17.40	17.73	18.22	17.12	17.44
Cr ₂ O ₃	0.00	0.00	0.00	0.00	0.00	0.00	0.00	0.00	0.00	0.00	0.00	0.00	0.00	0.00
FeO	0.00	0.00	0.00	0.00	0.06	0.00	0.00	0.16	0.00	0.02	0.00	0.03	0.00	0.03
MnO	0.03	0.00	0.05	0.00	0.00	0.00	0.03	0.00	0.05	0.00	0.00	0.02	0.04	0.09
MgO	0.02	0.02	0.03	0.00	0.00	0.01	0.04	0.01	0.00	0.00	0.00	0.02	0.01	0.02
CaO	0.05	0.00	0.00	0.04	0.04	0.01	0.03	0.02	0.00	0.00	0.04	0.01	0.00	0.00
Na ₂ O	0.20	0.15	0.29	0.23	0.28	0.36	0.15	0.22	0.18	0.21	0.24	0.17	0.25	0.24
K ₂ O	16.18	15.77	16.14	16.03	16.17	15.95	16.12	15.82	16.43	16.01	16.32	15.32	15.87	16.12
BaO	0.22	0.18	0.06	0.00	0.36	0.44	0.07	0.17	0.03	0.03	0.12	0.09	0.23	0.09
Total	98.88	98.81	99.04	98.76	99.09	99.15	98.53	98.55	98.35	98.45	99.43	100.56	98.40	98.85
Structural formula based on 8 oxygens														
Si	3.041	3.058	3.030	3.051	2.992	3.011	3.021	3.015	3.015	3.034	3.017	3.038	3.044	3.028
Ti	0.000	0.001	0.000	0.000	0.001	0.001	0.001	0.000	0.001	0.001	0.005	0.000	0.000	0.002
Al	0.945	0.935	0.961	0.939	1.006	0.984	0.974	0.984	0.976	0.961	0.972	0.978	0.946	0.961
Cr	0.000	0.000	0.000	0.000	0.000	0.000	0.000	0.000	0.000	0.000	0.000	0.000	0.000	0.000
Fe ²⁺	0.000	0.000	0.000	0.000	0.003	0.000	0.000	0.006	0.000	0.001	0.000	0.001	0.000	0.001
Mn ²⁺	0.001	0.000	0.002	0.000	0.000	0.000	0.001	0.000	0.002	0.000	0.000	0.001	0.001	0.004
Mg	0.001	0.001	0.002	0.000	0.000	0.000	0.003	0.001	0.000	0.000	0.000	0.001	0.001	0.001
Ca	0.003	0.000	0.000	0.002	0.002	0.001	0.020	0.001	0.000	0.000	0.002	0.000	0.000	0.000
Na	0.018	0.014	0.026	0.021	0.025	0.033	0.014	0.020	0.017	0.019	0.021	0.015	0.023	0.022
K	0.965	0.937	0.960	0.954	0.965	0.950	0.964	0.946	0.987	0.957	0.968	0.890	0.950	0.962
Ba	0.004	0.003	0.001	0.000	0.007	0.008	0.001	0.003	0.001	0.001	0.002	0.002	0.004	0.002
Total	4.978	4.949	4.983	4.967	5.000	4.988	4.980	4.976	4.998	4.973	4.987	4.926	4.969	4.982
An	0.254	0.000	0.000	0.189	0.187	0.071	0.164	0.119	0.000	0.000	0.196	0.027	0.000	0.000
Ab	1.830	1.425	2.667	2.103	2.568	3.342	1.392	2.049	1.674	1.982	2.156	1.668	2.347	2.221
Or	97.916	98.575	97.333	97.708	97.245	96.587	98.444	97.831	98.326	98.018	97.648	98.305	97.653	97.779

Beam size is given in micrometer

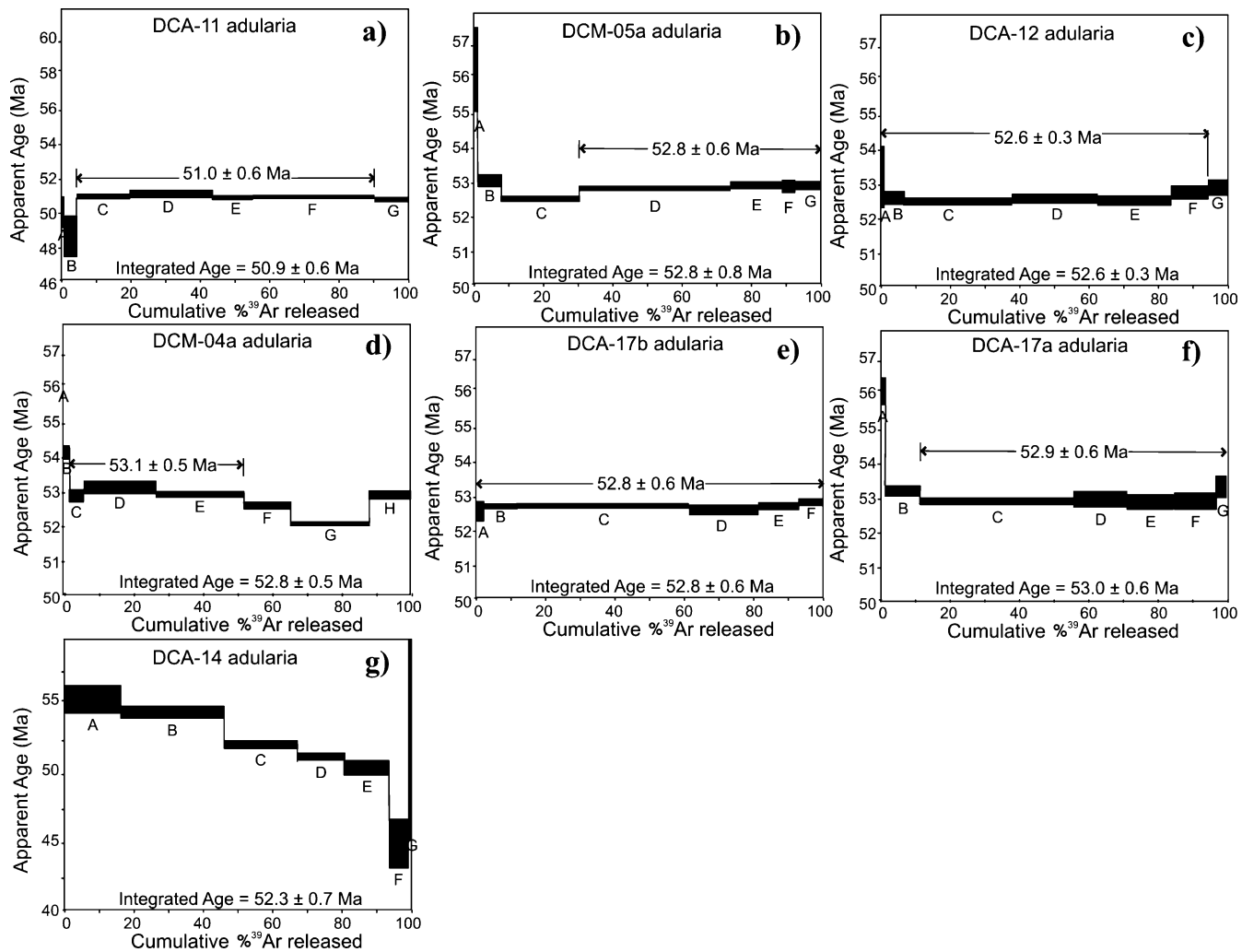


Fig. 5 Conventional $^{40}\text{Ar}/^{39}\text{Ar}$ age spectra of hydrothermal adularia samples

Table 4 $^{40}\text{Ar}/^{39}\text{Ar}$ analytical data of hydrothermal adularia from the El Peñon deposit

Step	Laser Pwr	$^{36}\text{Ar}/^{39}\text{Ar}$	$^{37}\text{Ar}/^{39}\text{Ar}$	$^{38}\text{Ar}/^{39}\text{Ar}$	$^{40}\text{Ar}*/^{39}\text{Ar}$	Mol ^{39}Ar	$^{40}\text{Ar}^*$ (%)	Age (Ma)	$\pm (2\sigma)$
DCA-11, Carmín Inferior (underground, 7302400N, 450600E)									
A	3	0.374	0.096	0.406	51.907	0.011	32.000	50.09	0.46
B	6	0.026	0.136	3.309	50.394	0.070	87.000	48.65	0.60
C	10	0.002	0.081	0.597	52.890	0.284	99.200	51.02	0.06
D	13	0.001	0.139	0.188	53.041	0.443	99.700	51.17	0.11
E	16	0.008	0.093	0.131	52.839	0.213	95.700	50.97	0.06
F	20	0.001	0.193	0.071	52.875	0.653	99.700	51.01	0.04
G	30	0.001	0.877	0.047	52.671	0.190	99.300	50.81	0.06
Plateau age 51.0 ± 0.6 Ma (85% released gas); MSWD=0.87; $J=0.0005411 \pm 0.0000032$									
Inverse isochron age 51.0 ± 0.6 Ma, $n=4$, $^{40}\text{Ar}/^{39}\text{Ar}$ intercept 288 ± 10 , MSWD=0.84									
DCM-05A, Qda. Colorado (underground)									
A	2	0.244	0.011	0.055	25.161	0.080	25.900	56.22	0.62
B	5	0.002	0.000	0.042	23.695	0.552	98.100	52.99	0.71
C	8	0.000	0.000	0.042	23.457	1.826	99.500	52.47	0.04
D	10	0.000	0.000	0.041	23.604	3.544	99.600	52.79	0.03
E	12	0.000	0.000	0.041	23.633	1.220	99.500	52.85	0.06
F	15	0.001	0.001	0.041	23.627	0.294	98.400	52.84	0.08

Table 4 (continued)

Step	Laser Pwr	$^{36}\text{Ar}/^{39}\text{Ar}$	$^{37}\text{Ar}/^{39}\text{Ar}$	$^{38}\text{Ar}/^{39}\text{Ar}$	$^{40}\text{Ar}^*/^{39}\text{Ar}$	Mol ^{39}Ar	$^{40}\text{Ar}^*$ (%)	Age (Ma)	$\pm (2\sigma)$
G	30	0.002	0.000	0.041	23.641	0.590	98.100	52.87	0.06
Plateau age 52.8±0.8 Ma (70% released gas); MSWD=0.00; $J=0.0012550\pm 0.0000098$									
Inverse isochron age 52.8±0.8 Ma, $n=5$, $^{40}\text{Ar}/^{39}\text{Ar}$ intercept 336±19, MSWD=0.90									
DCA-12, Carmín Inferior (underground, 7302400N, 450600E)									
A	3	0.140	0.047	0.065	49.384	0.016	54.400	53.28	0.44
B	6	0.001	0.008	0.050	48.814	0.082	99.600	52.67	0.10
C	10	0.000	0.002	0.042	48.698	0.461	99.900	52.55	0.05
D	13	0.000	0.002	0.042	48.784	0.360	99.800	52.64	0.07
E	16	0.000	0.001	0.045	48.722	0.310	99.900	52.57	0.06
F	20	0.001	0.001	0.043	48.959	0.160	99.700	52.83	0.10
G	30	0.001	0.002	0.042	49.078	0.068	99.600	52.95	0.11
Plateau age 52.6±0.3 Ma (95% released gas); MSWD=1.39; $J=0.0006055\pm 0.0000036$									
Inverse isochron age 52.4±0.6 Ma, $n=5$, $^{40}\text{Ar}/^{39}\text{Ar}$ intercept 1100±200, MSWD=0.11									
DCM-04A, Qda. Colorado (underground)									
A	2	0.081	0.012	0.016	27.312	0.008	53.400	57.59	0.72
B	5	0.001	0.001	0.021	25.693	0.112	98.400	54.22	0.10
C	8	0.000	0.000	0.023	25.063	0.298	99.900	52.91	0.94
D	11	0.000	0.001	0.044	25.190	1.518	99.900	53.18	0.09
E	14	0.000	0.000	0.043	25.095	1.810	99.900	52.98	0.04
F	18	0.000	0.000	0.043	24.934	0.968	99.900	52.65	0.05
G	24	0.000	0.000	0.042	24.674	1.640	99.900	52.10	0.03
H	30	0.000	0.000	0.044	25.084	0.834	99.900	52.96	0.06
Plateau age 53.1±0.5 Ma (50% released gas); MSWD=0.00; $J=0.0011848\pm 0.0000054$									
Inverse isochron age 52.9±0.4 Ma, $n=5$, $^{40}\text{Ar}/^{39}\text{Ar}$ intercept 730±40, MSWD=2.10									
DCA-17b, Carmín Inferior (underground, 7302375N, 450600E)									
A	3	0.036	0.005	0.055	48.133	0.085	81.900	52.64	0.15
B	6	0.000	0.006	0.043	48.275	0.412	99.700	52.79	0.04
C	10	0.000	0.002	0.043	48.281	2.089	99.900	52.80	0.03
D	13	0.000	0.005	0.041	48.177	0.840	99.800	52.69	0.07
E	16	0.001	0.007	0.044	48.273	0.491	99.700	52.79	0.05
F	30	0.000	0.005	0.041	48.385	0.289	99.700	52.91	0.06
Plateau age 52.8±0.6 Ma (100% released gas); MSWD=1.24; $J=0.0006137\pm 0.0000036$									
DCA-17A Carmín Inferior (underground, 7302375N, 450600E)									
A	3	0.009	0.163	0.049	49.389	0.025	94.900	56.14	0.20
B	6	0.001	0.015	0.043	46.752	0.155	99.700	53.19	0.07
C	10	0.000	0.004	0.043	46.493	0.653	99.900	52.90	0.04
D	13	0.000	0.005	0.041	46.538	0.230	99.900	52.95	0.11
E	16	0.000	0.003	0.043	46.468	0.200	99.900	52.87	0.10
F	22	0.000	0.002	0.044	46.491	0.184	99.800	52.90	0.12
G	30	0.001	0.033	0.037	46.851	0.040	99.500	53.30	0.16
Plateau age 52.9±0.6 Ma (88% released gas); MSWD=1.23; $J=0.0006385\pm 0.0000038$									
DCA-14, Carmín Inferior (underground, 7302400N, 450600E)									
A	3	0.863	0.021	0.100	47.828	0.034	15.800	55.06	0.48
B	6	0.011	0.029	0.199	46.967	0.063	93.300	54.08	0.18
C	10	0.008	0.018	0.090	44.991	0.044	94.800	51.84	0.14
D	13	0.015	0.010	0.046	44.222	0.029	90.800	50.96	0.15
E	16	0.047	0.009	0.045	43.511	0.026	75.700	50.16	0.27
F	22	0.463	0.140	0.047	38.730	0.012	22.000	44.71	0.86
G	30	1.343	1.885	0.017	47.300	0.001	10.600	54.46	4.79

$J=0.0006464\pm 0.0000038$

Data in italics were excluded in inverse isochron analysis

Laser Pwr Power of laser in watt

$^{40}\text{Ar}^*$ is radiogenic ^{40}Ar

phyries, porphyritic pyroxene–hornblende–biotite monzonites, and hornblende–biotite dacite porphyries), which were emplaced within and around the early diorite plutons in the Cerro Paisaje area. These Lower Eocene porphyry intrusives mark the end of the magmatism in the basin and a change to a compressive tectonomagmatic regime.

Magmatic and mineralization events in the El Peñon deposit

Adularia samples yield good plateau ages in most selected samples and appear to have been undisturbed because crystallization and cooling from initial low hydrothermal temperatures. However, McDougall and Harrison (1999) and Love et al. (1998) caution that $^{40}\text{Ar}/^{39}\text{Ar}$ dates from alkali feldspar may be difficult to interpret. Adularia generally crystallizes in the thermal stability field of triclinic microcline, but commonly has the metastable monoclinic structure because its rapid crystallization inhibits ordering of Si and Al. During slow cooling, Na-bearing K-feldspar may unmix and may also reorder to a more triclinic structure. Both unmixing and reordering may allow argon loss and result in a closure temperature as low as $\sim 150^\circ\text{C}$ (Love et al. 1998; McDougall and Harrison 1999). In this study, electron microprobe analyses indicate low albite contents (1.2. to 3.3 mol%) in adularia, and we infer rapid cooling (and low temperature of formation) deduced from the habitat in which adularia crystallized (veins and open spaces) and from fluid inclusion studies. In this case, unmixing and reordering, and consequent argon loss would be insignificant. Additionally, no exsolution textures were observed in optical petrographic and microprobe studies, or in the age spectra (lack of U-shaped spectra).

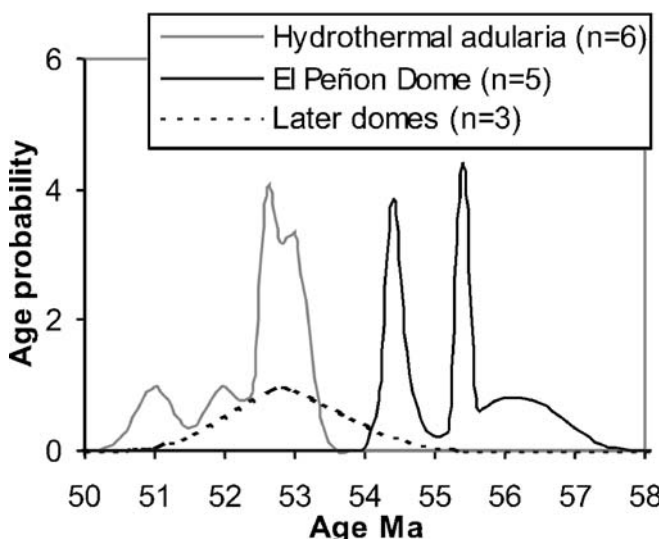


Fig. 6 Probability distribution for magmatic and hydrothermal events occurred in the El Peñon deposit (see text for details)

Well-defined plateau ages obtained in this study show that argon loss was insignificant and that this analytical method can be successfully used for adularia formation in short-pulse epithermal veins, as suggested by several workers (e.g., Groff et al. 1997; Love et al. 1998; Parsons et al. 1999; Sanematsu et al. 2004). Slight excess argon has been detected in some of the analyzed samples, but it does not appear significant when interpreting the age results. The best age estimates range between 53.1 ± 0.5 and 51.0 ± 0.6 Ma for adularia precipitation, apparently in two distinct pulses at $53\text{--}52.5$ and 51 Ma. Previous K–Ar ages of 53.5 ± 2.2 and 59.4 ± 1.4 Ma (Pérez 1999) for adularia in the El Peñon mine may reflect an excess argon component or a sample cleaning problem.

Au–Ag bearing quartz–adularia veins are partly hosted by and spatially associated with a rhyolite dome complex (El Peñon Dome), although some veins are emplaced in surrounding volcanic sequences. The obtained $^{40}\text{Ar}/^{39}\text{Ar}$ biotite age of 54.5 ± 0.6 for the El Peñon Dome is concordant within error with previous K–Ar (55.8 ± 1.5 and 56.5 ± 1.5 Ma) and U/Pb (55.4 ± 0.2 and 54.4 ± 0.2) ages (Pérez 1999; Cornejo et al. 2003). A later magmatic stage in the El Peñon deposit, represented by minor dacitic to rhyodacitic domes is documented in this study, which have K–Ar ages between 52.2 ± 1.8 and 53.7 ± 1.9 Ma.

Figure 6 shows a probability distribution which contains the $^{40}\text{Ar}/^{39}\text{Ar}$ and K–Ar ages for the El Peñon Dome, later bodies and hydrothermal adularia obtained in this study, and previous K–Ar (Pérez 1999) and U/Pb ages (Cornejo et al. 2003). Probability diagrams are based on the assumption that errors in a date have a Gaussian distribution, and the sum of the individual Gaussian curves are plotted (Deino and Potts 1992). For this reason, $^{40}\text{Ar}/^{39}\text{Ar}$ and U/Pb ages, which are analytically more precise than K–Ar ages, are associated with higher age probability. The data suggest that the later dacitic to rhyodacitic domes were emplaced 1 to 2 Ma. after the main rhyolitic complex, contemporaneously with adularia precipitation (Fig. 6).

Modelling studies (e.g., Cathles et al. 1997) suggest that near-surface hydrothermal activity hotter than 200°C can be sustained by a single intrusion event for less than 800,000 years; this period decreases drastically in silicic systems. According to these authors, longer-lived geothermal systems are likely to be associated with a series of short-lived pulses of intrusion and hydrothermal circulation. Geochronological data from the El Peñon area suggest that the period of ore formation postdates emplacement of the host rhyolitic dome by 1 to 2 Ma, and that mineralization is likely related to the latest minor dacitic–rhyodacitic bodies identified in the area. Mineralization was probably generated by at least two short-lived pulses related to single magmatic events, before the change in magmatic style represented by Lower Eocene intrusives located on the eastern boundary of the basin.

Acknowledgments Regional geological mapping and geochronology of volcanic and plutonic units were carried out under the auspices of the Servicio Nacional de Geología y Minería—Central Depression Project (P.C.). Fieldwork and dating of adularia samples were financially supported by a Postdoctoral Fondecyt Project 3030002 (G.A.). We thank the Meridian Gold Company for providing support, access to the mine and permission to publish these results. Comments by two anonymous reviewers and R.W. King as Associate Editor improved the manuscript. Mauricio Belmar (Universidad de Chile) collaborated with the SEM and EMPA study. Eugenia Fonseca, Marcelo Yáñez, and César Vásquez assisted with XRD and K–Ar analyses at Laboratory of the Servicio Nacional de Geología y Minería (Chile).

References

- Arancibia G, Matthews S, Pérez de Arce, C (2006) K–Ar and $^{40}\text{Ar}/^{39}\text{Ar}$ geochronology of supergene processes in the Atacama Desert, northern Chile: tectonic and climatic relations. *J Geol Soc (Lond)* 163:107–118
- Cathles LM, Erendi AH, Barrie T (1997) How long can a hydrothermal system be sustained by a single intrusive event? *Econ Geol* 92:766–771
- Chesley JT, Halliday AN, Snee LW, Mezger K, Sherperd TJ, Scrivener RC (1993) Thermochronology of the Cornubian batholith: implications for pluton emplacement and protracted hydrothermal mineralization. *Geochim Cosmochim Acta* 57:1817–1837
- Cornejo P, Matthews S (2001) Evolution of Magmatism from the Uppermost Cretaceous to Oligocene, and its relationship to changing tectonic regime, in the Inca de Oro–El Salvador area (northern Chile). In: III South American Symposium on Isotope Geology, Soc Geol Chile, Santiago, Chile, Extended Abstracts 558–561
- Cornejo P, Matthews S, Pérez de Arce C (2003) The “K–T” Compressive Deformation Event in Northern Chile (24–27°). In: 10º Congreso Geológico Chileno, Concepción Chile (CD-Rom)
- Deino AL, Potts R (1992) Age probability spectra for examination of single-crystal $^{40}\text{Ar}/^{39}\text{Ar}$ dating results: examples from Olorgesailie, southern Kenya rift. *Quat Int* 13/14:47–53
- Dong G, Morrison GW (1995) Adularia in epithermal veins, Queensland: morphology, structural state and origin. *Mineralium Deposita* 30:11–19
- García F (1967) Geología del Norte Grande de Chile. In: Simposium sobre el Geosinclinal Andino. Soc Geol Chile Pub 3:p138
- Groff J, Heizler, Matthew T, McIntosh William C, Norman DI (1997) $^{40}\text{Ar}/^{39}\text{Ar}$ dating and mineral paragenesis for Carlin-type gold deposits along the Getchell trend, Nevada: evidence for cretaceous and tertiary gold mineralization. *Econ Geol* 92:601–622
- Love D, Clark A, Hodgson C, Mortensen J, Archibald D, Farrar E (1998) The timing of adularia–sericite-type mineralization and alunite–kaolinite-type alteration, Mout-Skukum epithermal gold deposit, Yukon territory, Canada. $^{40}\text{Ar}/^{39}\text{Ar}$ and U–Pb geochronology. *Econ Geol* 93:437–462
- McDougall I, Harrison T (1999) Geochronology and thermochronology by the $^{40}\text{Ar}/^{39}\text{Ar}$ method, 2nd edn. Oxford University Press, p 269
- McKee E, Noble D (1989) Cenozoic tectonic events, magmatic pulses, and base and precious-metal mineralization in the Central Andes. In: Erickson GE, Cañas Pinochet MT, Reinemund JA (eds). *Geology of the Andes and its relation to hydrocarbon and mineral resources*. Houston, Texas, Circum-Pacific Council for Energy and Mineral Resources Earth Sciences Series 11:189–194
- Marinovic N, Smoje I, Maksaev V, Hervé M, Mpodozis C (1995) Hoja Aguas Blancas, Región de Antofagasta, Carta Geológica de Chile N° 70, escala 1:250.000. Ser Nac de Geol Min, Santiago
- Marinovic N, García M (1999) Hoja Pampa Unión, Región de Antofagasta, Mapa Geológico de Chile N° 9, escala 1:100.000. Ser Nac de Geol Min, Santiago
- Parsons I, Brown WL, Smith JV (1999) $^{40}\text{Ar}/^{39}\text{Ar}$ thermochronology using alkali feldspars: real thermal history or mathematical mirage of microtexture? *Contrib Mineral Petrol* 136:92–110
- Pérez M (1999) Alteración Hidrotermal en el Depósito Epitermal de Au–Ag El Peñón, II Región, Antofagasta. Memoria de título (thesis), Universidad de Chile, p 109
- Robbins CH (2000) Geology of the El Peñón gold–silver deposit, northern Chile. In: *Geology and ore deposits 2000: the Great Basin and beyond*. JK Cluer, JG Price, EM Struhsacker, RF Hardyman, and CL Morris (eds) *Geology Society of Nevada Symposium Proceedings* p 219–232
- Sanematsu K, Watanabe K, Duncan R, Izawa E (2004) Mineralization ages using $^{40}\text{Ar}/^{39}\text{Ar}$ dating and the precipitation of gold in the Hishikari epithermal gold deposit, Japan. In: International Association of Volcanology and Chemistry Earth's Interior (IAVCEI) General Assembly, Pucón, Chile. Abstr (CD-Rom)
- Sébrier M, Lavenu A, Fornari M, Soulard JP (1988) Tectonics and uplift in Central Andes (Peru, Bolivia and northern Chile) from Eocene to present. *Geodynamique* 3:85–106
- Scheuber E, González G (1999) Tectonics of the Jurassic–Early Cretaceous magmatic arc of the north Chilean Coastal Cordillera (22°–26°S): a story of crustal deformation along a convergent plate boundary. *Tectonics* 18:895–910
- Sillitoe R, McKee E, Vila T (1991) Reconnaissance K–Ar geochronology of the Maricunga gold–silver belt, northern Chile. *Econ Geol* 86:1261–1270
- Sillitoe R, McKee E (1996) Age of supergene oxidation and enrichment in the Chilean porphyry copper province. *Econ Geol* 21:164–179
- Tomlinson A, Blanco N (1997) Structural evolution and displacement history of the west fault systems, Precordillera, Chile: part 1, synmineral history. In: VIII Congreso Geológico Chileno, Antofagasta, III:1873–1877
- Warren I, Zuluaga J, Robbins C, Wulfang W, Simmons S (2004) Geology and geochemistry of epithermal Au–Ag mineralization in El Peñón district, northern Chile. In: Sillitoe RH, Perelló J, Vidal CE (eds) *Andean metallogeny: new discoveries, concepts, and updates*. Soc Econ Geol Spec Publ 11:113–139